

Analysis of flow and density oscillations in a swirl-stabilized flame employing highly resolving optical measurement techniques

Andreas Fischer · Jörg König · Jürgen Czarske ·
Johannes Peterleithner · Jakob Woisetschläger ·
Thomas Leitgeb

Received: 15 April 2013 / Revised: 1 October 2013 / Accepted: 15 October 2013 / Published online: 30 October 2013
© Springer-Verlag Berlin Heidelberg 2013

Abstract Modern aircraft engines operate with a reduced core air mass flow, which is challenging regarding an efficient and most of all stable combustion of fuel. A variable geometry burner investigated here allows a stable lean combustion with lower air mass flow rate than with a fixed geometry. In order to optimize such burners further, the occurring flame instabilities have to be investigated. This requires optical measurement techniques with a high measurement rate and an insensitivity regarding flame glow. Concerning flow velocity measurements, the frequency modulated Doppler global velocimetry (FM-DGV) fulfills these demands. In the swirl-stabilized flame of the variable geometry burner, spectra up to 2.5 kHz of the flow velocity field were obtained with FM-DGV. For example, a resonance peak at about 255 Hz was identified in the swirled flame, which also occurs in complementing density measurements by laser interferometric vibrometry. The combined analysis of velocity and density oscillations offer new insights into the physics of flame flows.

1 Introduction

In recent years, emission restrictions have forced the industry to focus on cleaner combustion rather than solely on maximum efficiency. Emission of unburnt hydrocarbon, soot and NO_x is of particular interest. The latter increases with flame temperature. Low NO_x strategies usually include lean combustion in order to reduce the flame temperature. As a drawback, local flame extinction cannot be avoided completely. This effect causes a fluctuation of heat release, which again interacts with pressure variations. Under certain conditions, this interaction can occur periodically as thermo-acoustic coupling, a reason why new lean-premix combustion systems tend to have oscillations. This is a major problem for gas turbine manufacturers because it leads to lower power output—an economical problem, or in worst case, component damage. Efforts have been made in order to understand and model instabilities (Lieuwen 2003). However, the effect has still not been fully understood.

Simultaneously, active and passive control mechanisms have been developed to approach the problem. Passive systems employing acoustic dampers only decrease the amplitude of certain frequencies, while active systems are more flexible but also increase the grade of complexity (Dowling and Morgans 2005). Despite the problems, lean combustion is state of the art (Lefebvre 1999). Since reliable prediction of instabilities is still not possible, the devices are modified after they have been designed. This is very costly, and therefore, a strong need for predictive tools is evident.

Another aspect of modern gas turbine design is part load capability. While gas prices increase and renewables gain ground, gas turbines are operated well off their design point. This changes the flow field considerably. As a consequence,

A. Fischer (✉) · J. König · J. Czarske
Laboratory for Measurement and Testing Techniques,
Department of Electrical Engineering and Information
Technology, Technische Universität Dresden, Helmholtzstr. 18,
01062 Dresden, Germany
e-mail: andreas.fischer2@tu-dresden.de

J. Peterleithner · J. Woisetschläger · T. Leitgeb
Institute for Thermal Turbomachinery and Machine Dynamics,
Graz University of Technology, Inffeldgasse 25A,
8010 Graz, Austria

the combustion process faces either flame blow out or the flame attaches to the injector tip and increases the temperature of the structure. The situation can be avoided either by turning off several burners and keeping the remaining ones turned on full load or by employing variable geometry burners such as the one investigated in this paper. The former has the disadvantage of a non-uniform circumferential temperature profile hitting the first turbine stage, while the latter can maintain a homogeneous distribution. In the variable geometry burner, tangential air is mixed with fuel, in an annular mixing chamber, when the mixture flows further to the center, it is diluted with the axial air. By varying the ratio of axial to tangential air, the swirl of the premixed flame is adjusted. By reducing the exit area after the mixing zone, the exit velocity can be adjusted in order to avoid a diffusion flame or flame blow out. With a variable geometry burner, a stable combustion can be maintained with 50 % reduced mass flow compared to the design point (Giuliani et al. 2012).

This finding was obtained from measurements in a model combustor. Equipped with an appropriate liner, the damping of combustion oscillations can be investigated. Without the liner, it provides maximum access for optical measurement systems. Hence, the experiments in a model combustor are an advantageous alternative to cost-intensive experiments in large-scale combustion laboratories.

Since the model combustor is swirl-stabilized and this concept is commonly employed in gas turbines, it allows the study of typical combustion effects of gas turbines. The swirl eases ignition and stabilizes operation. Generally, swirl combustors form a recirculation zone, bringing hot gas back into the flame region where it helps igniting the fresh fuel–air mixture, which arrives from the injector. The recirculation is driven by vortex breakdown. This breakdown is defined as a flow instability due to the formation of an internal stagnation point located on the vortex axis where a reverse flow region establishes (Leibovich 1978). Centrifugal instabilities and Kelvin–Helmholtz instabilities can be found in this region as well (Wang et al. 2005).

In order to deepen the understanding of combustion instabilities, local and time-resolved information of state variables is necessary. Swirl-stabilized flames are characterized by highly turbulent effects, which make prediction of their behavior difficult. Numerical simulation has been tried for years, but while direct numerical simulation (DNS) is well beyond a reasonable run duration, the commonly applied Reynolds averaged Navier–Stokes (RANS) technique cannot provide temporally resolved data. Consequently there is a high demand for measurement techniques, capable of high acquisition rates. Ongoing developments have pushed the maximum detectable oscillation frequencies to 100 kHz for density fluctuation measurements using the laser interferometric vibrometry (LIV) system and

50 kHz for the frequency modulated doppler global velocimetry (FM-DGV). Both systems are rather new, but validation has been performed and can be found in the literature (Leitgeb et al. 2013; Fischer et al. 2009). However, FM-DGV was not applied to flame flows so far.

The aim of this paper is to enhance the knowledge about the flow characteristics and especially combustion instabilities in the variable geometry burner operated with a lean combustion. As one key aspect, the FM-DGV technique is applied to flame flow measurements for the first time in order to obtain flow velocity spectra. First, the variable geometry burner is described in Sect. 2 Next, the setup of the applied measurement systems is explained in Sect. 3 The measurement results are subsequently discussed in Sects. 4 and 5. Finally, the important conclusions are drawn and an outlook will be presented in Sect. 6.

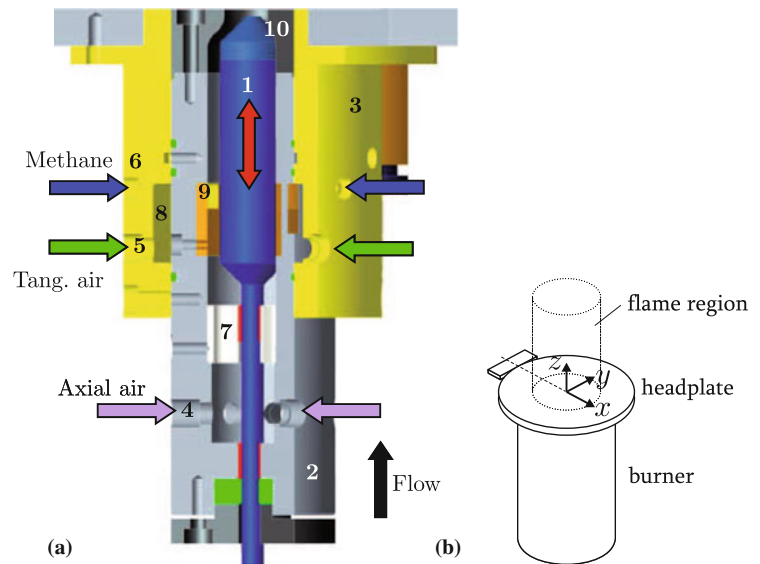
2 Burner concept

The variable geometry burner depicted in Fig. 1a basically consists of three main parts: a movable center-body (1) which can be moved ± 3 mm axially, an inner (2), and an outer bushing (3). The six connectors for the axial air (4) are mounted at the inner bushing, while the outer bushing has six connectors for the tangential air (5) and four connectors for the fuel supply (6). Here, methane is used as fuel. The axial air is forced into purely axial direction by a flow straightener (7) before mixing between air and fuel is performed in the cavity (8) of the outer bushing. The inner bushing has also four tangential inlet slots (9) for introducing the swirl to the flow. In order to adjust the momentum of the swirl flow into the cavity, the entries can be blocked with inserts. The size of the inserts has been set to obtain equal momentum in axial and swirl flow at the mixing zone. The exit area of the injector nozzle (10) is altered by the axial position of the center-body. The tip of the center-body and the nozzle shape can be changed easily in order to investigate different nozzle geometries. The ratio of the inner diameter of the injector nozzle and the outer diameter of the center-body controls both the mixture velocity and the bluff body effect of the center-body.

The stratifier stratifies the axial air. This is necessary, because the axial air is supplied by six radial feed lines in the lower section of the burner. By means of the stratifier, the axial air flow is forced into a purely axial direction.

Hence, the desired operation conditions can be adjusted by setting the swirl strength (changing the ratio of tangential to axial air) and the overall air mass flow rate (changing the area cross-section of the injector nozzle exit). The chosen coordinate system with respect to the burner is shown in Fig. 1b. Throughout all tests, the burner is operated vertically.

Fig. 1 **a** Layout of the variable geometry burner (Giuliani et al. 2012) and **b** the chosen coordinate system. The diameter of the headplate amounts to 100 mm



3 Measurement concept

3.1 Visualization

The flame shapes are visualized at different operating points by measuring the light emission of CH^* -radicals. These emissions indicate the flame front in premixed flames (De Leo et al. 2003, 2007). Using a Thorlabs blue filter FGB25S centered at 380 nm and with 130 nm full width at half maximum, the flame radiation is photographed from 18 directions on a half revolution by turning the burner in steps of 10° between each shot. For each direction, 300 frames are recorded with a Panasonic NV-DX100E video camera. Finally, the 3d flame front is obtained by the tomographic reconstruction technique described in Herman (2009) using the software program IDEA (Hipp et al. 1999, 2004).

3.2 Stereoscopic particle image velocimetry (SPIV)

In order to describe the aerodynamics in the midplane of the flame, measurements by means of stereoscopic particle image velocimetry (SPIV) are performed. The SPIV setup is depicted in Fig. 2. It is similar to the one presented in reference (Giuliani et al. 2010).

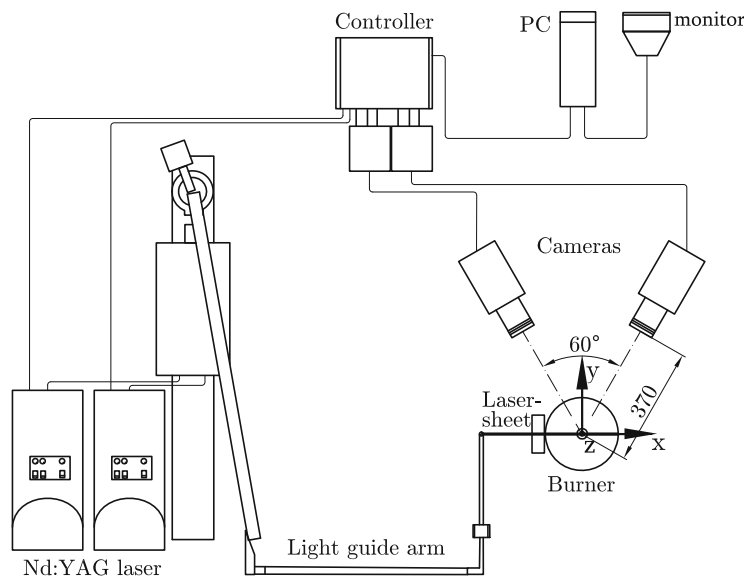
The measurement system consists of a laser light source, two CCD cameras, a controller and a personal computer (PC). As laser light source a pulsed Nd:YAG laser (New Wave GEMINI) producing laser bursts at a wavelength of 532 nm is used. The pulse duration is 3–5 ns with a maximum energy of 120 mJ at a repetition rate of 15 Hz. Two temporally narrow laser bursts with a time interval of 100 μs are generated by using two separate laser-resonators (double cavity). A light guide arm and a light sheet probe

(spherical lens with 600 mm focal length, cylindrical lens with -10 mm focal length) are used for generating a light sheet at $y = 0$ with 2 mm in thickness. Due to the rather large light sheet thickness, the measured flow field is spatially averaged in axial direction. This spatial averaging has to be taken into account when discussing the measurement results. The cameras are of type 80C60 HiSense (Dantec Dynamics), which have a resolution of $1,280 \times 1,024$ pixels, a bit depth of 12 bit and are operated in the double-frame mode. They are mounted on a Scheimpflug mount and use AF-Micro Nikkor 60/2.8 lenses. Interference filters centered at 532 nm with a bandwidth of 10 nm are used to damp the flame glow which would have caused overexposed images otherwise. For the synchronization of laser bursts and cameras, a separate controller (FlowMap 1500, Dantec Dynamics) is applied. The controller is connected with a computer for final data evaluation and visualization (FlowManager 4.60.28). The illuminated field of view is about $50 \text{ mm} \times 37 \text{ mm}$ in the x - z -plane. The window size amounts to 32×32 pixel, which corresponds to a lateral spatial resolution of $1.25 \text{ mm} \times 1.25 \text{ mm}$. The lateral spatial resolution is similar to spatial resolution of the FM-DGV measurements.

Although interference filters are applied, the thermal light emission of the flame still influences the camera images. In order to obtain a sufficient number of validated vectors, 1,200 image pairs are acquired per operating point, which means a measurement time of 80 s.

As tracer particles, titanium dioxide (TiO_2) particles from DuPont with an average size of $0.4 \mu\text{m}$ are used together with a seeding generator of type PivSolid 3 from PivTec GmbH. According to PivTec, the size of the output seeding particles amounts to 0.5 – $1 \mu\text{m}$. These particles are injected into the axial air supply of the burner shortly

Fig. 2 Stereoscopic PIV setup



before the air distribution box. According to (Albrecht et al. 2003), the slip of, e.g., 1 μm spherical particles of TiO₂ is lower than 1 % up to flow oscillations with 1.6 kHz frequency. This is considered to be sufficient for the investigations here.

3.3 FM-DGV

The FM-DGV technique relies on measuring the Doppler frequency shift f_D of laser light, which is scattered by seeding particles moving with the flow (Fischer et al. 2011):

$$f_D = \underbrace{\vec{v} \cdot \frac{\vec{\sigma} - \vec{i}}{|\vec{\sigma} - \vec{i}|}}_{=\vec{s}} \cdot \frac{|\vec{\sigma} - \vec{i}|}{\lambda} \quad (1)$$

with λ as laser wavelength, $\vec{\sigma}$ as observation direction and \vec{i} as laser incidence direction. Hence, the velocity component $v_{oi} = \vec{v} \cdot \vec{s}$ along the direction of the sensitivity vector \vec{s} (i.e., along the bisecting line of $\vec{\sigma}$ and $-\vec{i}$) can be derived from the measured Doppler frequency.

Using a continuous laser illumination, high measurement rates can be achieved if seeding particles are present in the measurement volume at any time. With the current FM-DGV system, measurement rates up to 100 kHz are possible, so that velocity spectra with maximum 50 kHz bandwidth can be measured with FM-DGV in principle (Fischer et al. 2009). In practice, however, a temporal averaging is often applied for reducing the measurement uncertainty. Despite this, measurement rates of several kilohertz are typically feasible. The key challenge is to keep the signal-to-noise ratio high enough, so that the

measurement uncertainty remains smaller than the flow oscillations in order to be able to detect them.

3.3.1 Illumination

For achieving a high signal-to-noise ratio, a high-power laser at 895 nm is used as laser source. It is a distributed feedback diode laser with a subsequent power amplifier from Toptica Photonics AG delivering about 0.5 W via a single-mode fiber. The fiber output is collimated with an aspherical lens providing a beam with about 1 mm in diameter in the measurement region. The laser center frequency coincides with an atomic resonance of cesium gas and, thus, the laser is stabilized to the cesium D₁ absorption line at 335.11370 THz (Fischer et al. 2011). Details concerning the stabilization technique are given in Fischer et al. (2009).

3.3.2 Observation

As seeding particles, the same kind of TiO₂ particles are used as for the SPIV measurement. For receiving the Doppler-shifted scattered light, the measurement plane is imaged through another absorption cell filled with cesium gas onto an array of 24 fiber-coupled avalanche photodiodes as depicted in Fig. 3a. The 24 measurement points are aligned along the laser beam in a linear arrangement, while the observation direction $\vec{\sigma}$ is always perpendicular to the laser incidence direction \vec{i} , i.e., $|\vec{\sigma} - \vec{i}| = \sqrt{2}$. Using multimode fibers with a diameter of 400 μm that are coupled with the avalanche photodiodes, the optical magnification of the receiving unit results in a lateral dimension of the detection volume of about 1 mm. The depth of field of the receiving unit amounts to 13 mm,

while the numerical aperture is about 0.08 and the working distance is 140 mm.

3.3.3 Determining the Doppler frequency

In order to measure the Doppler frequency, the FM-DGV measurement principle relies on applying a sinusoidal laser frequency modulation (FM) and evaluating the amplitude ratio $q = A_1/A_2$ of the first- and second-order harmonic of the detector signals. Such harmonics do occur due to the sinusoidal laser frequency modulation and the nonlinear spectral transmission profile of the cesium absorption cell as illustrated in Fig. 3b. As a result, the amplitudes A_1 , A_2 are a function of the Doppler-shifted laser center frequency and the mean scattered light power, while the latter cancels when calculating the amplitude ratio q .

The chosen amplitude of the sinusoidal laser frequency modulation is about 320 MHz, which is approximately 55 % of the full width at half maximum of the transmission curve (590 MHz) to achieve minimum measurement uncertainty (Fischer et al. 2007). The modulation period time is 10 μ s. The calculation of the amplitudes A_1 , A_2 of the first- and second-order harmonic at 100 and 200 kHz, respectively, is based on a Fourier analysis of each detector output signal using Fast Fourier Transform. Further details about the FM-DGV measurement principle, the measurement system and about calibrating the relation between the amplitude ratio q and the velocity v_{oi} can be extracted from Fischer et al. (2007, 2008).

3.3.4 Three component field measurements

According to Eq. (1), three measurement configurations are (sequentially) applied for obtaining all three velocity components:

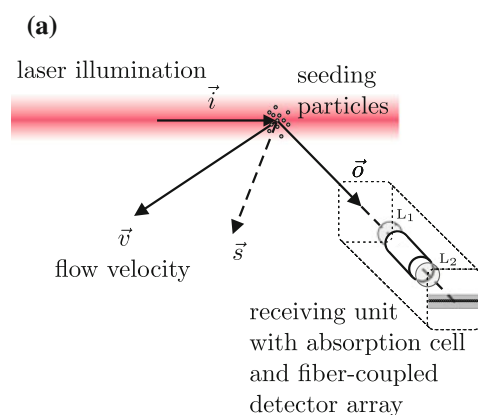


Fig. 3 **a** Sketch of the FM-DGV setup (linear detection, lenses L_1 and L_2 for imaging) and **b** illustration of the sinusoidal laser frequency modulation with the period time $1/f_m$ (bottom) around the

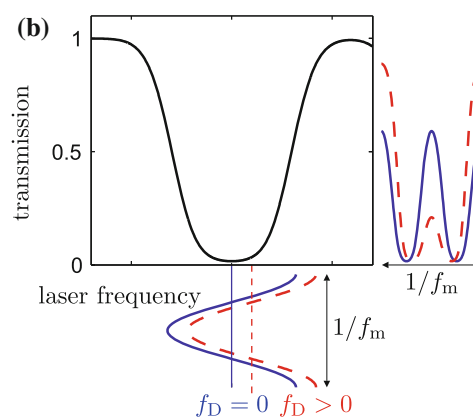
- In configuration 1, which is depicted in Fig. 4a, the incidence direction and the observation direction are perpendicular. According to the sketch and Eq. (1), the measured velocity component v_1 equals v_x .
- For configuration 2, the burner is turned by -90° around the burner axis. This is shown in Fig. 4b and results in $v_2 = v_y$.
- Contrary to v_x and v_y , the third component v_z is not obtained directly. According to configuration 3, which is depicted in Fig. 4c, the observation angle is turned by 34° . As a result, the measured velocity v_3 is a mixture of the desired orthogonal components and, thus, v_z is finally obtained by a coordinate transform of v_1 , v_2 and v_3 . Since the three original components are measured sequentially, a coordinate transform can only be applied for the velocity mean values.

The array measurement points are always aligned along the illuminating laser beam and centered to the burner center. The flow field in the x – y -plane is obtained by traversing the burner as indicated in Fig. 4a–c in steps of 2 mm. The vertical position of the burner is adjusted to measure the flow field at $z = 25$ mm and $z = 35$ mm.

3.3.5 Spatial resolution

According to the described illumination and observation setup, the lateral and axial dimension of the detection volume is larger or equal to the laser beam diameter and, thus, the available laser power in the detection volumes is maximized. As a further consequence, the lateral and axial spatial resolution amounts to about 1 mm due to the dimension of the intersecting volume of the illuminated volume and the observed volume.

Regarding the experiment, the spatial resolution of the measurement system is similar to the Kolmogorov length



atomic resonance of cesium gas at 895 nm and the resulting transmittance (right) in case of no Doppler shift ($f_D = 0$, blue solid lines) and a positive Doppler frequency ($f_D > 0$, red dashed lines)

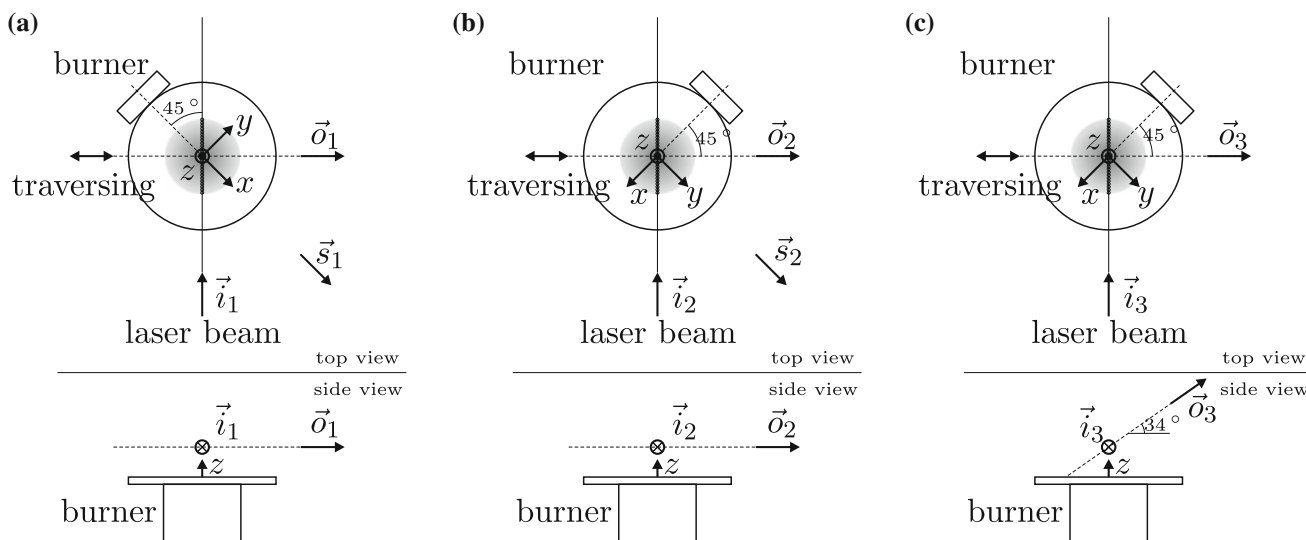


Fig. 4 Arrangements for measuring three velocity components v_1, v_2, v_3 with the following sensitivity directions: **a** $\vec{s}_1 = (100)^T$, **b** $\vec{s}_2 = (010)^T$, **c** $\vec{s}_3 = (0.0855, 0.9145, 0.39541)^T$. The *rectangle* marks the orientation of the burner

scale. When defining $L = k^{3/2}/\epsilon$ as length scale characterizing the large eddies with k as turbulent kinetic energy and ϵ as dissipation rate, the Kolmogorov length scale η_K that is valid for isotropic turbulence reads (Pope 2000)

$$\eta_K = \frac{L}{Re_t^{3/4}} \tag{2}$$

with $Re_t = \frac{k^{1/2}L}{\nu}$ as turbulence Reynolds number and ν as kinematic viscosity. As a result, the Kolmogorov length scale is >0.6 mm for $L \approx 0.02$ m (radial extent of the swirled flow), $\nu \approx 180 \times 10^{-6}$ m²/s (fluid viscosity at 1,000 °C), $k < 1$ m²/s² (based on measurements). Hence, most of the flow structures are assumed to be spatially resolved when neglecting the anisotropy of the flow turbulence.

3.3.6 Measurement rate and temporal resolution

The chosen period time of the laser frequency modulation of 10 μ s enables measurement rates up to 100 kHz, because at least one modulation period is required for determining the amplitudes A_1, A_2 . However, the achieved seeding concentration limits the actual achievable measurement rate to a few kilohertz. For this reason, a measurement rate of 5 kHz is used here, i.e., 20 subsequent modulation periods are evaluated at once corresponding to a temporal resolution of 200 μ s.

Note that the chosen measurement rate of 5 kHz is sufficient with respect to the resolvable flow velocity oscillations. For the spatial resolution of $\Delta s = 1$ mm and mean flow velocities $|\bar{u}| < 5$ m/s (approximation based on measurements), the acquired flow velocity oscillations have frequencies $< \frac{|\bar{u}|}{2\Delta s}$, i.e., < 2.5 kHz, when applying the

frozen flow hypothesis and the spatial sampling theorem. Consequently, a measurement rate of 5 kHz is sufficient for the given spatial resolution according to the temporal sampling theorem.

Regarding the Kolmogorov length scale η_K for isotropic turbulence and the Taylor frozen turbulence hypothesis (Pope 2000), the maximum frequency of a flow velocity oscillation reads

$$f_K = \frac{|\bar{u}|}{\eta_K} \tag{3}$$

The resulting cutoff frequency is 8.3 kHz here, which is higher than the maximum resolvable frequency of 2.5 kHz. For the present flame experiment, however, the dominant flow oscillations are expected to occur at frequencies < 2.5 kHz. For further future studies, the spatial and the temporal resolution have to be improved.

3.3.7 Cross-sensitivity with respect to the flame and particle glow

Since harmonics of the detector signals are evaluated, ambient light does not disturb the measurement (i.e., no systematic error occurs) if the ambient light fluctuation between one period of the laser frequency modulation is negligible. The latter holds for our experiment. The insensitivity of the FM-DGV measurement principle with respect to ambient light is a unique feature in comparison with other DGV techniques. This feature is similar to, e.g., laser Doppler anemometry, where only the alternating component of the detector signal is evaluated as well (Albrecht et al. 2003). In contrast to common laser Doppler anemometers, however, the FM-DGV system provides simultaneous

measurements at multiple points with a high measurement rate, which allows spatiotemporal correlation analyses.

Although ambient light causes no systematic error, the elements of the detector array can still be saturated or the random error can increase due to the shot noise from the ambient light (Seitz 2007). The saturation of the photo detection unit and the increased detector noise are well-known disturbances, which also occur with laser Doppler anemometry or PIV. In order to eliminate or to reduce these disturbances, respectively, a narrow band-pass filter is usually applied in front of the receiving unit. The band-pass filter attenuates the ambient light from the flame and the glowing of the seeding particles. Here, a band-pass filter with a center wavelength of 895 nm and a bandwidth of 20 nm) is used for the FM-DGV measurements. The effect of the band-pass filter is demonstrated in Fig. 5 by showing a sample detector signal with and without filter while seeding is on and the laser is off. Considering all detector channels, an average reduction in the ambient light of 92 % is achieved from 3.4 nW to 0.27 nW.

In order to illustrate the improvement by using the band-pass filter in terms of a signal-to-noise ratio (SNR), a typical mean power of the scattered laser light of 1 nW is now considered as a numerical example. This means an incident laser light power of approximately 0.25 nW, because of the sinusoidal laser frequency modulation, the approximately parabolic shape of the transmission profile of the absorption cell and the amplitude of the frequency modulation being approximately one half of the absorption line width. Furthermore, the noise equivalent power NEP due to thermal noise, dark current noise, shot noise and avalanche gain excess noise reads

$$NEP = \sqrt{NEP_{min}^2 + b \cdot P} \tag{4}$$

with the constants $NEP_{min} = 39 \text{ fW/Hz}^{1/2}$, $b = 1.49 \times 10^{-18} \text{ W/Hz}$ and P as mean incident light power on the

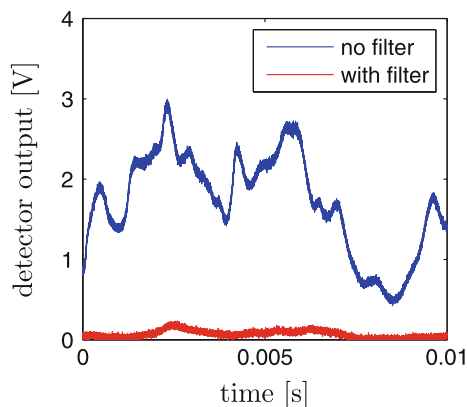


Fig. 5 Effect of the band-pass filter to suppress the ambient light (laser is off)

detector (Fischer et al. 2008). Applying Eq. (4) and comparing the NEP^2 values for the different cases (a) flame exposure without band-pass filter ($P = 0.25 \text{ nW} + 3.4 \text{ nW}$), (b) flame exposure with band-pass filter ($P = 0.25 \text{ nW} + 0.27 \text{ nW}$) and (c) without flame exposure ($P = 0.25 \text{ nW}$) finally yields the following conclusions regarding the SNR: With the band-pass filter, the SNR is improved by a factor of 3. However, the SNR is still 18 % lower than the SNR without flame exposure. Thus, the flame glow and the particle glow increase the measurement uncertainty.

3.3.8 Sample signal and measurement uncertainty

A sample detector signal in case of a running laser system (modulated laser frequency) is shown in Fig. 6. The fast modulation due to the laser frequency modulation as well as slow variations of the scattered light power can be seen. The latter fluctuations occur, e.g., due to a varying number of seeding particles in the measurement volume. Fluctuations of the scattered light power can lead to a measurement uncertainty. However, the resulting uncertainty can usually be neglected for mean flow velocities $< 40 \text{ m/s}$ (Fischer et al. 2008), which applies for the flame flow experiment.

Considering only random errors, the standard deviation of the flow velocity mainly results from thermal noise, dark current noise, shot noise and avalanche excess noise of the photo detector as well as from fluctuations of the laser center frequency (Fischer et al. 2008, 2009). The resulting velocity standard deviation σ_{v_i} of the i th velocity component as obtained by error propagation calculations and validated by experiments reads

$$\sigma_{v_i} \approx \frac{1}{\sqrt{T/s}} \times \sqrt{(1 + k_{glow,i}) \cdot \frac{(0.0084 \text{ m/s})^2}{(P_{s,i}/\text{nW})^2} + \frac{(0.0051 \text{ m/s})^2}{P_{s,i}/\text{nW}} + (0.003 \text{ m/s})^2} \tag{5}$$

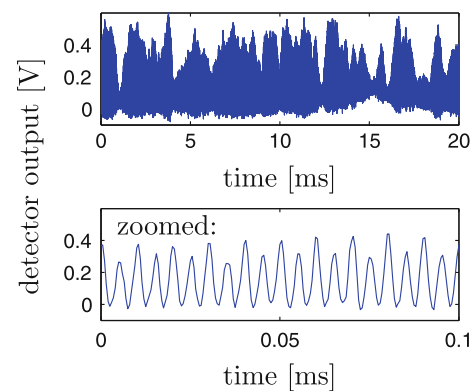


Fig. 6 Modulation of the detector signal (measurement sample)

with $P_{s,i}$ as scattered laser light power and T as measurement time (Fischer et al. 2009, 2010). The first summand is due to thermal noise and dark current noise, the second summand is due to shot noise and avalanche excess noise and the third summand is due to error contributions, which are independent of the scattered laser light power (e.g., fluctuations of the laser center frequency). The original formula is enhanced by $k_{\text{glow},i} \geq 0$ in order to take the noise increase due to the flame glow and the particle glow into account. The quantity $k_{\text{glow},i}$ is the noise power increase normalized by the noise power in case of no flame glow, no particle glow and no laser signal. Using Eq. (4), one obtains

$$k_{\text{glow},i} = \frac{b \cdot P_{\text{glow},i}}{\text{NEP}_{\text{min}}^2}, \quad (6)$$

where $P_{\text{glow},i}$ is the incident light power on the detector due to the flame and particle glow. Note that the portion of $P_{\text{glow},i}$ caused by particle glow is directly proportional to the number of seeding particles in the measurement volume. The same proportionality is valid for $P_{s,i}$ and, thus, both light powers are not independent from each other.

During the flame flow experiment, average light powers of the scattered laser light $P_{s,i}$ of about 1.6 nW, 2 nW and 0.6 nW are achieved at $z = 25$ mm for the three configurations, respectively. For convenience, we use $P_{\text{glow},i} \approx 0.3$ nW based on the band-pass filter experiment, i.e., $k_{\text{glow},i} \approx 0.3$. Furthermore, the measurement time T is 50×1 s at each position. Thus, it follows from Eq. (5) $\sigma_{v_1} \approx 1.1$ mm/s, $\sigma_{v_2} \approx 0.9$ mm/s, $\sigma_{v_3} \approx 2.5$ mm/s. While these random errors are negligible for the evaluation of the larger velocity mean values, they are relevant for resolving the small fluctuations of the flow velocity as is discussed in Sect. 5.1

In addition to the random error, a systematic error of about ± 0.5 m/s is determined by repeated calibration measurements. The calibration measurements are performed at a rotating glass disk, where the tangential velocity is given by the radial measurement position and the rotation frequency (Fischer et al. 2007). The origin of the systematic error are assumed to be mainly variations of the temperature of the absorption cell, because the absorption cell temperature influences the spectral transmission profile of the absorption cell (Fischer et al. 2008). Although the absorption cells are temperature stabilized, deviations from the set temperature do exist. Furthermore, drifts of the amplitude of the sinusoidal laser frequency modulation or drifts of the laser center frequency could contribute to the measured systematic error. The systematic error is larger than the random error and, thus, limits the measurement performance regarding the measurement of mean flow velocities. However, the systematic error is not

relevant when considering oscillations of the flow velocity with frequencies >1 Hz, because the time constant of the systematic effects is larger than several minutes.

3.4 Laser interferometric vibrometry (LIV)

For complementing and supporting the data of the flow velocity oscillations obtained with FM-DGV, laser interferometric vibrometry (LIV) is also applied providing the mean power spectrum of flow density fluctuations. LIV has already been demonstrated to be a useful tool for flame diagnostics (Giuliani et al. 2006, 2010; Lang et al. 2008; Köberl et al. 2010). The measurement principle relies on correlating the output signals of two intersecting laser vibrometers in order to extract the commonly measured flow density fluctuations at the intersection point (Hempel and Woisetschlager 2006; Köberl et al. 2010). LIV provides high measurement rates up to 250 kHz, and thus, fast oscillations of flow density can be identified at a single point. One aspect of the application of LIV is also to characterize the relation between flow velocity oscillations (measured with FM-DGV) and flow density oscillations (measured with LIV). Note that the LIV measurements are separately performed without seeding particles after the FM-DGV measurements.

Two laser vibrometers from the company Polytec are used consisting of the sensing head (OFV-353) and the controller (OFV-3001). They are operated in the velocity decoding mode. Further settings for the laser vibrometers are shown in Table 1. The carrier frequency of both laser vibrometers is 40 MHz. In front of the apertures, collimation lenses are mounted with focal lengths of -40 mm forming parallel laser beams with diameters of 2 mm. Mirrors are placed at the opposite side of the measurement volumes in order to reflect the object beams back to the apertures. The perpendicular arrangement of both laser vibrometers is illustrated in Fig. 7a. The intersection point of both beams is the measurement position. A photo of the two intersecting laser beams is shown in Fig. 7b. Data acquisition is done with an I/O board of type BNC 2110 (National Instruments). The software programs for data acquisition and controlling the laser vibrometers are programmed with LabVIEW.

Again, the burner is traversed for scanning the measurement area. The measurements take place at $x \in [-15 \text{ mm}, 15 \text{ mm}]$, $y \in [-15 \text{ mm}, 15 \text{ mm}]$ for two heights: $z = 25$ mm and 35 mm. The spacing between two measurement points is 2.5 mm. At each point, 786,432 samples with a sampling frequency of 16,384 Hz are recorded, which equals a measurement time of 48 s. The 786,432 samples are divided into 384 parts with 2,048 samples. According to the measurement principle, an averaging over

384 spectra is applied, which are calculated out of 2,048 samples each.

4 Flame characterization

In Fig. 8, the flame shape regimes are presented as a function of the reduced mass flow and the equivalence ratio for both, fixed geometry (FG) and variable geometry (VG) operation of the burner.

The default operating point (design point) is indicated by a black dot. It is located in the non-shaded green area, which indicates the regime of a lifted flame employing fixed geometry. By reducing the overall air mass flow rate and keeping the equivalence ratio as well as the geometry parameters constant, the operating point shifts to the left toward the attached flame regime (blue and red area). The blue area shaded with dashed lines indicates the increased operation range for the lifted flame regime by employing variable geometry. Comparing the transitions from lifted to attached flame regimes for fixed geometry (FG) and variable geometry (VG), respectively, variable geometry enables to sustain a stable lifted flame up to approx. Fifty percentage of the air mass flow rate met at the transition boundary for fixed geometry.

The subsequently tested burner operation conditions are listed in Table 2. The given air split ratio is the ratio $\frac{\dot{m}_{\text{tan}}}{\dot{m}_{\text{main}}}$

Table 1 Settings of the laser vibrometers

Description	Value
Tracking filter	Off
Velocity range	5 mm/V/s
Velocity filter	Off
Displacement range	0.5 $\mu\text{m/V}$

between the tangential and the main air mass flow rate, and the injector area A is normalized by the area A_0 at the design point. The equivalence ratio is ϕ . The visualized flame shapes according to these conditions are shown in Fig. 9

Comparing A1 and A2 in Fig. 9 shows the influence of a higher swirl regarding the flame structure and position. In the case of a higher swirl, the flame flattens and moves toward the front plate. The change is dramatic given the low range of tangential air split rise (from 43.5 to 48.7 % of the main air). For the two cases B1, B2 at part load (reduced mass flow), the reduction in the inlet injection area leads to an increase in the air inlet velocity and forces the flame to detach and to stabilize in the far field.

These findings from flame visualization are complemented and enhanced by the mean velocity fields acquired with SPIV complement. In Fig. 10, the measured flow velocity fields (color code = absolute value of the velocity vector) are shown for the four operation conditions.

Considering A1, A2 and B2, the flame stabilizes at the place of strong velocity gradients and at the base of the swirling motion. In the case B1 of the jet flame, the front stabilizes on the inside and outside of the jet. Concerning the swirl number computed at 36 mm (which is two times the outer diameter of injector) over the front plate, they augment when the tangential air split increases (compare A1 and A2). In addition, it can be noticed that the swirling motion is stronger at part load (compare A1 and B1).

The turbulence level is computed as the ratio of the root mean square of the total velocity to the total velocity. For comparison, its minima corresponding to peak jet values are reported. The turbulence level is mostly a function of the reference inlet velocity. It rises dramatically from 25 to 50 % when reducing the inlet section hence augmenting the inlet velocity (compare A1 and B2). Higher swirl is related to a lower turbulence level (cases A2 and B1).

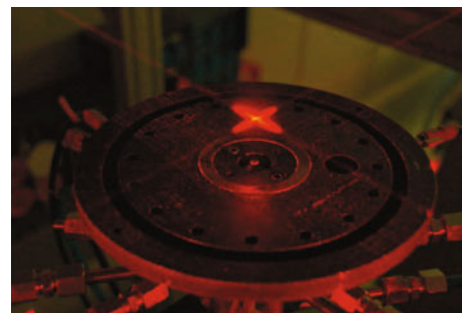
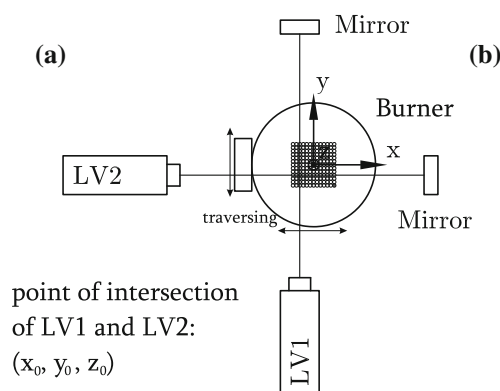


Fig. 7 **a** LIV measurement setup with two laser vibrometers: LV1 at $x = x_0$ and LV2 at $y = y_0$. The z -position equals z_0 for LV1 and LV2. Hence, the two laser beams intersect at (x_0, y_0, z_0) . The burner was

mounted on a traversing system for scanning the flow. **b** Photo of the intersecting laser beams for $x_0 = 0, y_0 = 0, z_0 = 25$ mm above the burner headplate

For the sake of completeness and for validation purposes, the mean velocity fields measured with FM-DGV are also presented in Fig. 11. The measurements were obtained at $z = 25$ mm and $z = 35$ mm for the design point operation (case A1). The expected swirl with counter clockwise orientation is clearly visible at both z -positions. The mean flow is radial symmetric except for some artifacts at the boundary, which is assumed to result from a lower seeding concentration and, thus, less reliable measurements. At $z = 25$ mm, an expected minimum of the z -component of the velocity occurs at the swirl axis. This kind of minimum is less pronounced at $z = 35$ mm.

For validating the FM-DGV measurements, the profiles of v_x with respect to the position x from the intersecting lines of the FM-DGV and SPIV measurement planes are compared with the SPIV results in Fig. 12a, b, respectively. v_x is discussed as an example while similar conclusions can be drawn for all velocity components. The error bars indicate the expanded uncertainty according to the international 'Guide to the Expression of uncertainty in measurements' (GUM) with a coverage factor of 2 (Lira 2002). According to the GUM, random and systematic errors are taken into account. Regarding the FM-DGV measurements, the standard deviation of the velocity mean value is always <0.02 m/s, and thus, the systematic error of ± 0.5 m/s mainly determines the measurement uncertainty (see Sect. 3.3). The standard uncertainty of the SPIV measurements is

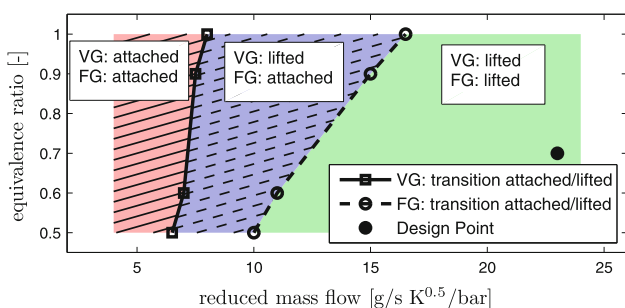


Fig. 8 Transition map of the flame regimes for fixed geometry (FG) at design point and variable geometry (VG)

Table 2 Operation conditions of the variable geometry burner

Operation point	Description	Thermal power (kW)	Corrected mass flow ^a (g/s)	Equivalence ratio ϕ	Air split ratio $\frac{\dot{m}_{air}}{\dot{m}_{min}}$ (%)	Injection area ratio $\frac{A}{A_0}$ (%)
A1	Design point	4	1.4	0.7	43.5	100
A2	A1, with elevated swirl	4	1.4	0.7	48.7	100
B1	A1, with 52 % less mass flow	2	0.73	0.7	45.7	100
B2	B1, with smaller inlet surface	2	0.73	0.7	45.7	65

^a Corrected for ISA conditions at sea level)

2 %. As a result of the low mean flow velocities <3 m/s, the uncertainty of the FM-DGV measurements is higher than the uncertainty of the SPIV measurements. The velocity profiles measured with FM-DGV and SPIV mainly coincide within the given confidences. Only at $x \approx 12$ mm, $z = 25$ mm a higher systematic deviation with maximum 1 m/s occurs. Several reasons are known for these systematic deviations:

- *Repeatability of the experiment:* Although using equal flow settings for both experiments, the operation conditions of the flow are assumed to differ slightly. The FM-DGV and SPIV measurements were performed at different times in a laboratory in Dresden and in Graz, respectively.
- *Non-identical measurement positions:* Beside mechanical adjustment issues, the incident incident laser light is deflected by refractive index gradients in the flame flow caused by temperature gradients. Considering the mean temperature distribution, a systematic deviation from the intended measurement position results. Stochastic temperature fluctuations are assumed to be negligible due to the long measurement durations. FM-DGV and PIV are affected by this disturbance in a different way, because of the different illumination and observation arrangements and the different sensitivity vectors for FM-DGV and SPIV. Currently, the magnitude of the error is difficult to determine, because the temperature distribution is not known.
- *Spatial averaging effects:* Due to the large light sheet thickness, the SPIV measurements include a stronger spatial averaging than the FM-DGV measurement. This could explain the higher deviation at $x \approx 12$ mm, $z = 25$ mm between FM-DGV and SPIV measurements, because the flow velocities measured with SPIV are lower

In conclusion, the FM-DGV measurement of the velocity mean values currently suffers from a (constant) systematic error that is not negligible with respect to the low mean flow velocities in the flame flow experiment.

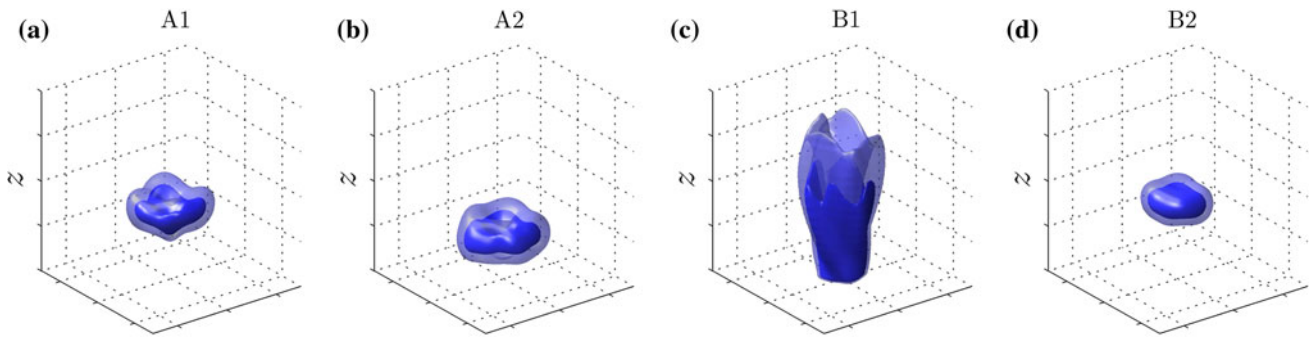


Fig. 9 Visualized flame shapes by two arbitrary isosurfaces of light intensity from CH* emission measurements at the four operation conditions **a** A1, **b** A2, **c** B1, **d** B2

Fig. 10 Velocity mean flow fields at $y = 0$ acquired with SPIV at the four operation conditions **a** A1, **b** A2, **c** B1, **d** B2. The *color* gives the absolute value of the velocity vector. Swirl number and turbulence level are A1: 0.36 and 30 %, A2: 0.47 and 26 %, B1: 0.47 and 25 %, B2: 0.33 and 51 %, respectively

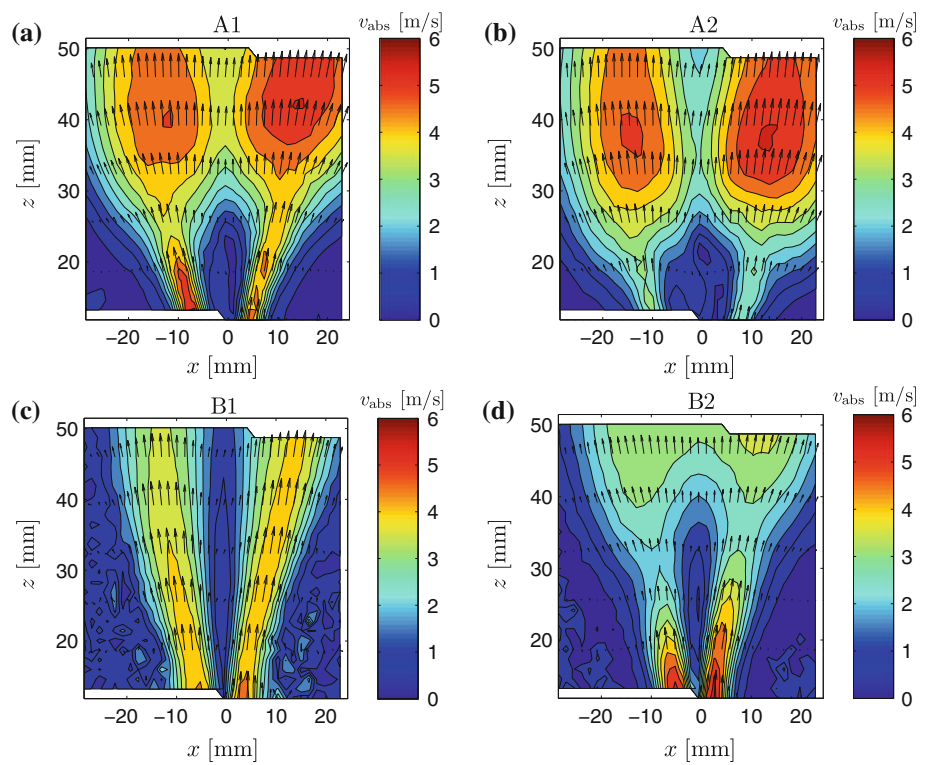


Fig. 11 Mean velocity fields measured with FM-DGV at **a** $z = 25$ mm and **b** $z = 35$ mm for the operation condition A1 (design point). The *color* represents the velocity component v_z

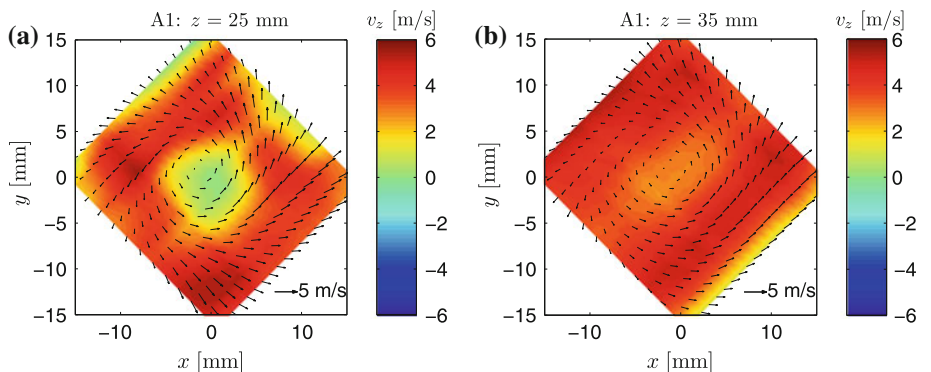
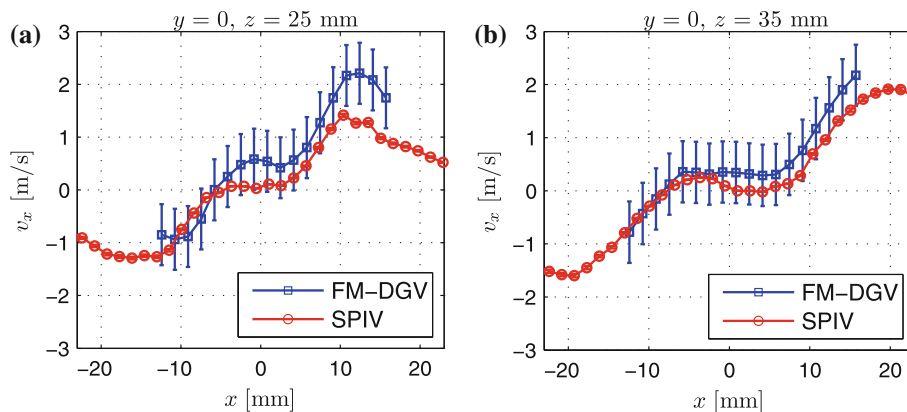


Fig. 12 Mean velocity profiles of v_x over x measured with FM-DGV and SPIV at $y = 0$ and **a** $z = 25$ mm and **b** $z = 35$ mm (intersecting lines of the different measurement planes). The error bars indicate the expanded uncertainty according to the international ‘Guide to the Expression of Uncertainty in Measurement’ (GUM) using a coverage factor of 2 (Lira 2002)



5 Flame dynamics

Flame dynamics are investigated further for the design point operation (case A1) using FM-DGV and LIV. With FM-DGV, velocity spectra were measured for detecting possible flow oscillations in the flame flow. These velocity fluctuations are finally compared with the density fluctuations measured with LIV.

5.1 FM-DGV for spectral characterization of velocity fluctuations

The interesting feature of FM-DGV is its capability to deliver velocity spectra up to several kilohertz for detecting possible flow oscillations. Here, a measurement rate of 5 kHz is used providing velocity spectra up to 2.5 kHz according to the sampling theorem. One velocity amplitude spectrum is calculated from 5000 samples using fast Fourier transform (which corresponds to a measurement time of 1 s) and is then averaged over 50 measurements. Note that only the original components v_1, v_2, v_3 can be analyzed here (and not v_x, v_y, v_z), because of the subsequent measurement of these components. Due to the chosen measurement arrangement, this allows to analyze $v_x = v_1$ and $v_y = v_2$, while $v_3 = f(v_x, v_y, v_z)$ contains portions of all three orthogonal velocity components. This limitation can be overcome in future, when having three receiving units with different observation directions operating in parallel instead of in succession.

First, velocity spectra of v_x along one measurement line at $z = 25$ mm are shown in Fig. 13a–l as an example. (The position of the measurement line is indicated in Fig. 14d.) A broad peak of 60 mm/s arises at 60 Hz in the swirl center (see Fig. 13g), which decreases off the burner axis. In addition, a flow velocity oscillation at about 255 Hz with narrower bandwidth occurs. Its amplitude becomes maximum 50–65 mm/s at approximately 8 mm off the burner

axis (Fig. 13c, k), where the swirl is maximum. In the swirl center, the oscillation at 255 Hz vanishes (Fig. 13g).

For higher frequencies, the spectral amplitude converges toward a certain value of about 10–20 m/s. This value results from flow oscillations and a bias of the spectrum estimation for low spectral amplitudes due to the random error of the FM-DGV measurements. Assuming a nominal spectral amplitude of zero and treating the random error as white noise, the bias can be estimated as follows: The average scattered laser light power is 1.6 nW yielding an estimated standard deviation of $\sigma_v \approx 0.55$ m/s for each velocity sample with a temporal resolution of $1/(5 \text{ kHz})$, see Eq. (5). Since one amplitude spectrum is calculated from $N = 5,000$ samples, the standard deviation of the real and imaginary parts of a Fourier coefficient equals $\sigma_v/\sqrt{2N}$ (Kay 1993). As a result, the square root of the expectation value of the squared absolute value (amplitude) of the complex Fourier coefficient leads to the bias $\sigma_v/\sqrt{N} \approx 8$ mm/s. The measured spectral amplitudes for high frequencies are closed to the estimated spectral bias value, but are typically higher. The higher value of the measured bias could result from the fact that the uncertainty of the velocity samples varies due to variations of the signal-to-noise ratio, but the velocity samples are currently treated equally weighted in the signal processing. This effect requires further investigations in future. In the present experiment, however, flow oscillations with amplitudes larger than the bias occur up to 1 kHz and, thus, can be resolved. Note that the systematic error of the FM-DGV system does not affect the measurements of the velocity spectra except for the direct component. Hence, only the random error limits the measurement uncertainty of the velocity spectra.

To study the spatial distribution of the magnitude of the identified flow oscillations at 60 and 255 Hz over the entire measurement area at $z = 25$ mm, the spectral amplitudes of the three velocity components v_x, v_y, v_z averaged over 50–80 and 230–280 Hz are given as a function of x and y in

Fig. 13 FFT amplitude spectra of v_x measured with FM-DGV (measurement rate 5 kHz) at positions along the indicated arrow in Fig. 14d with a position increment of 2 mm (flame condition A1)

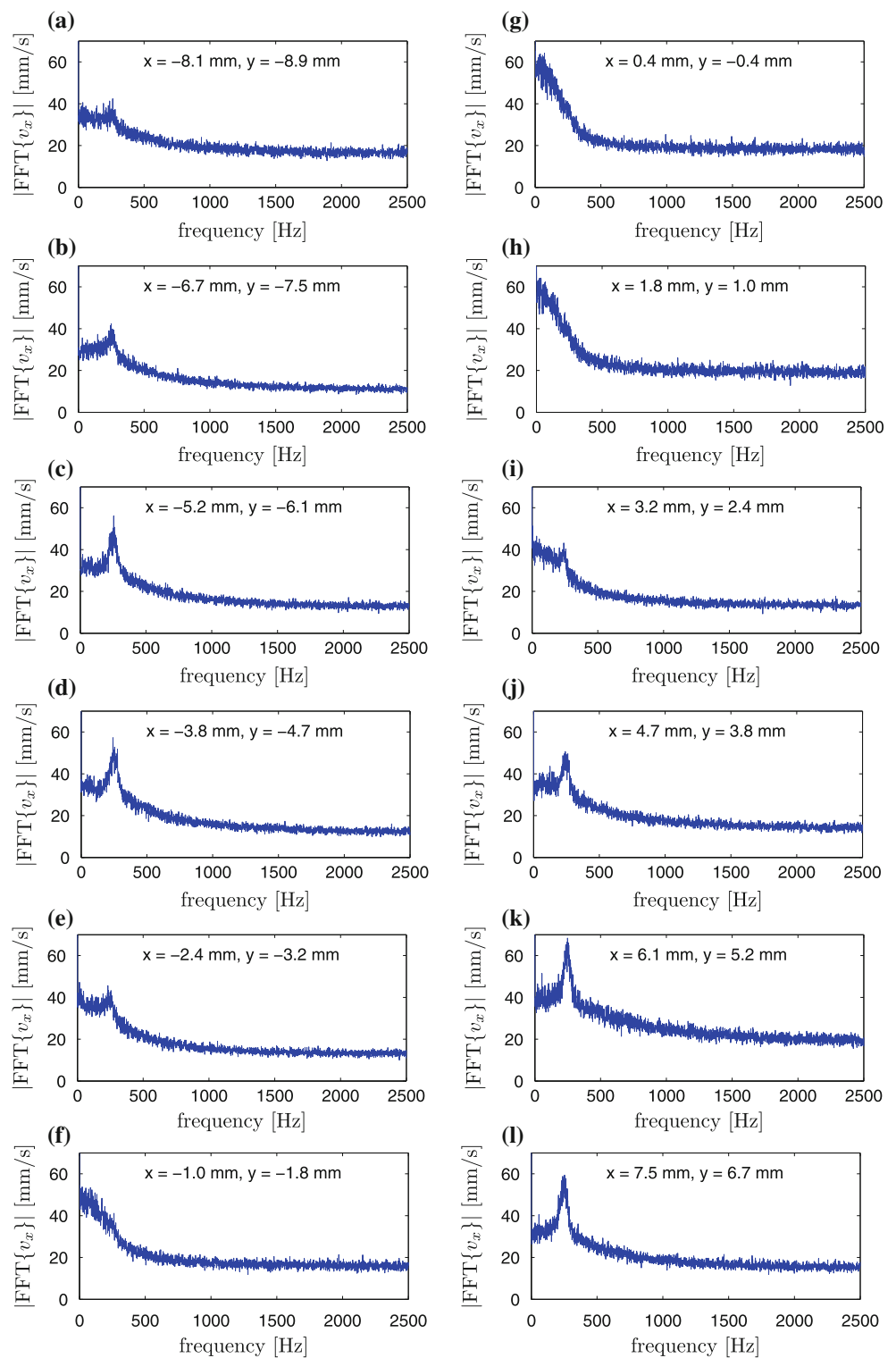
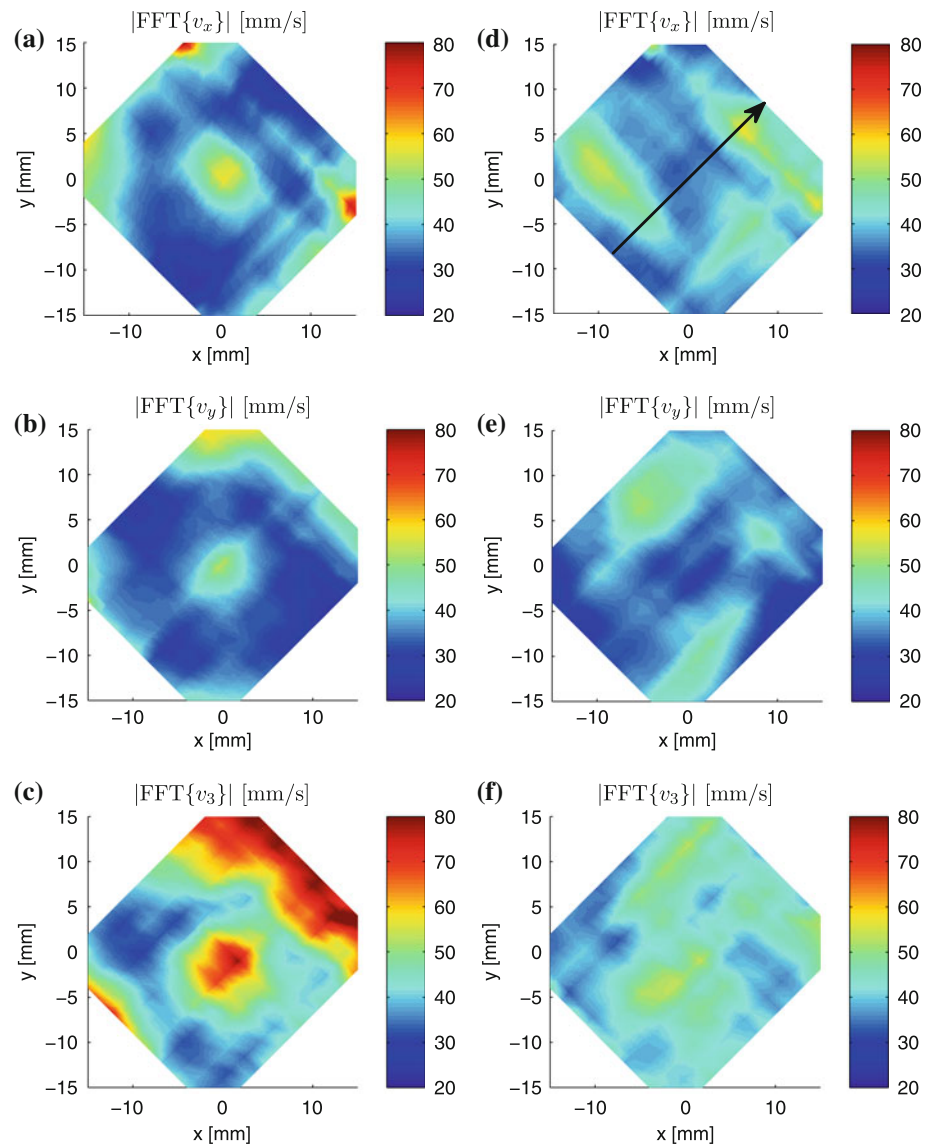


Fig. 14a–c (left) and in Fig. 14d–f (right), respectively. The amplitudes around 55 Hz (left) have a maximum at the burner axis. Additionally, the minimum is radial symmetric around the burner axis (swirl region). At the boundary, the amplitude sometimes increases. It is assumed that either the

processing vortex core or a highly unstable mixing of the flame flow with the surrounding air and a fluctuation of the swirl axis cause this behavior (Syred 2006). For about 255 Hz (right), the oscillation amplitudes are minimum in the flow center and contain maximum values at outer

Fig. 14 Mean FFT amplitude of v_x , v_y and v_3 at **a–c** 50–80 Hz and **d–f** 230–280 Hz at $z = 25$ mm measured with FM-DGV (measurement rate 5 kHz) at flame condition A1. The *arrow* in **d** indicates the positions of the velocity spectra shown in Fig. 13



regions. Mainly three maxima are visible for v_x and v_y rotated by 90° . It is assumed that this is a result of the tangential fuel supply arrangement (cf. Sect. 2) and the occurring burning oscillations interacting with the swirled flow. However, the reason of it has to be investigated further.

The data from $z = 35$ mm are not shown, because they contain no significant flow structures of the oscillations. It is very likely that the flow oscillations are smaller than the bias error there. In spite of this, FM-DGV already provided useful information about the oscillations in the flame flow.

5.2 LIV for spectral characterization of density fluctuations

Finally, the LIV measurement results are presented to complement the flow velocity fluctuation analysis with

information about density fluctuations. Two amplitude spectra of the density fluctuation are depicted in Fig. 15a from the flow center ($x = 0, y = 0, z = 25$ mm) and in Fig. 15b from the swirl region at the radial position 7 mm ($x = -5$ mm, $y = -5$ mm, $z = 25$ mm) as an example.

At the flow center, the spectrum contains a small resonance peak at about 450 Hz, which was not observed in the flow velocity spectra. In the frequency range 20–60 Hz, the amplitude becomes maximum. This peak is narrower than the peak in the velocity spectrum and, contrary to the velocity data, the peak is also present in the swirl region spectrum. As a result, the interaction between these density fluctuations and the corresponding velocity fluctuations remains unclear at first. However, the amplitude spectrum of the flow density from the swirl region has a peak at about 260 Hz, which is in excellent

Fig. 15 FFT amplitude spectra of ρ' from **a** the flow center ($x = 0, y = 0, z = 25$ mm) and **b** the swirl region ($x = -5$ mm, $y = -5$ mm, $z = 25$ mm) at flame condition A1

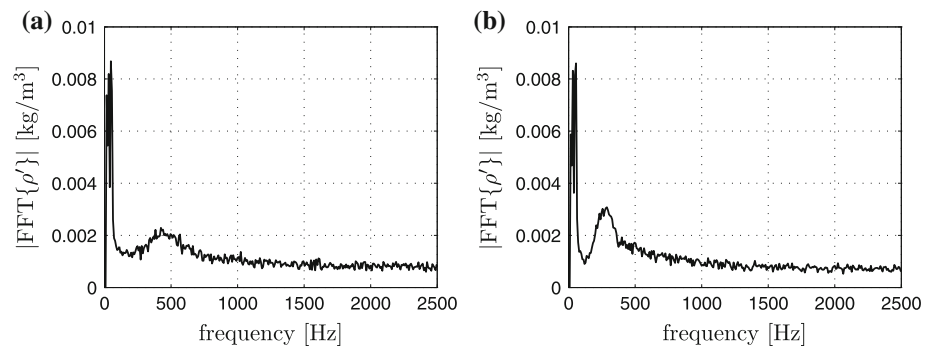
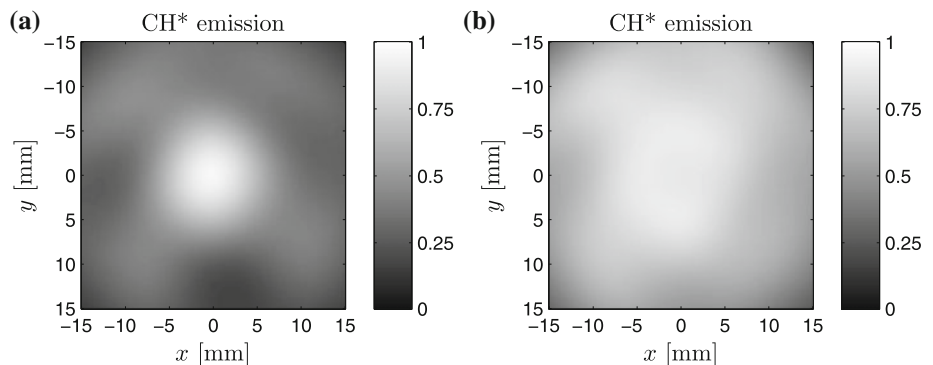


Fig. 16 CH* emissions at **a** $z = 25$ mm and **b** $z = 35$ mm normalized by the maximum value (flame condition A1)



agreement with the behavior of the flow velocity. Since density fluctuations are strongly correlated with temperature fluctuations due to combustion, the found flow fluctuations at about 255 Hz are obviously related to combustion fluctuations.

For comparing the density oscillations with the measured velocity oscillations at 50–80 Hz and 230–280 Hz further, the spatial distribution of the average amplitude of the density oscillations from the same frequency ranges are investigated subsequently. In order to take the heat release rate into account, the measured CH* emissions at $z = 25$ mm and $z = 35$ mm are given in Fig. 16a, b, respectively. CH* emissions depend on heat release, pressure and equivalence ratio (Nori and Seitzman 2009). For the atmospheric combustor with a fully premixed flame, the influence of the equivalence ratio and the pressure is assumed to be negligible and the CH* emission is proportional to the heat release rate.

The distributions of the average amplitude from 50 to 80 Hz at $z = 25$ mm and $z = 35$ mm are shown in Fig. 17a, b, respectively. At $z = 25$ mm, the density oscillation amplitude has a local maximum near the burner center. It decreases toward the boundary regions, which is in good agreement with the velocity behavior (cf. Fig. 14a–c). However, the central maximum of the density oscillation is smoother than that of the velocity oscillation. In addition, some maxima exist at the boundary, which are not present in the velocity data. Since these outer maxima and the minima in between appear symmetric with about 90°

around the burner axis, they are assumed to be caused by the symmetric fuel supply arrangement of the burner with four connectors. Indeed, the heat release rate shows a similar structure (see Fig. 16a). Note that the outer maxima of the density oscillations occur at minima of the heat release rate, while the central maximum of the density oscillations occurs at maximum heat release rate. At $z = 35$ mm, the structures of the density oscillations and the heat release rate (see Fig. 16b) are more homogeneous, because of the mixing of the flow. The density oscillation becomes minimum at the burner center and maximum at a ring structure with about 24 mm in diameter. The heat release rate mainly shows a broad maximum at the burner center. As a result, the low frequency density fluctuations off the burner center stem from larger-scale convection around the flame.

The average amplitudes of the density oscillation from 230 Hz to 280 Hz are shown in Fig. 18a, b, accordingly. At both heights, a minimum at the burner center and a ring structure with maximum amplitudes occur. At $z = 25$ mm for instance, the oscillation amplitude is maximum at a radius of about 7 mm. This ring structure widens for $z = 35$ mm to a radius of 10 mm and the oscillation amplitudes decrease. As a result, the high-frequency density fluctuations are strongest along the flame front and not in the areas of a high heat release rate. Furthermore, they occur together with flow velocity oscillations with equal frequency, although these velocity oscillations occur for different velocity components at different angular positions (cf. Fig. 14d–f). Hence, the identified velocity oscillations

Fig. 17 Mean FFT amplitude of the density ρ' over the frequency range 50–80 Hz at **a** $z = 25$ mm and **b** $z = 35$ mm measured with LIV (flame condition A1)

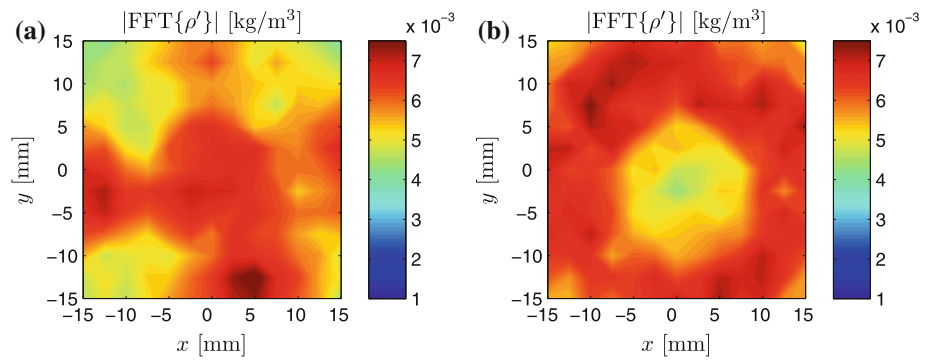
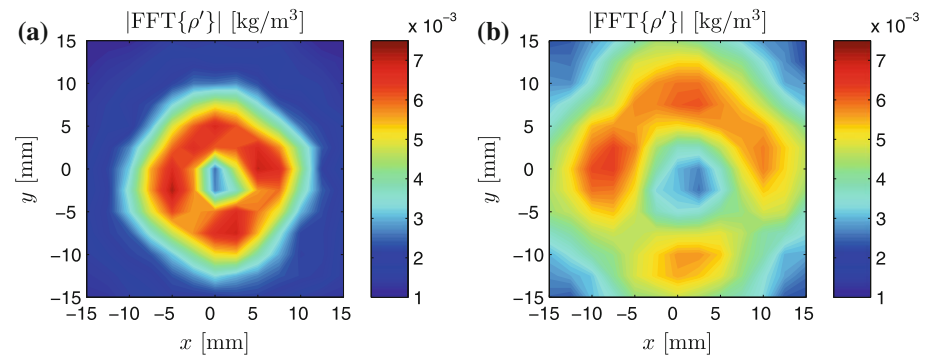


Fig. 18 Mean FFT amplitude of the density ρ' over the frequency range 230–280 Hz at **a** $z = 25$ mm and **b** $z = 35$ mm measured with LIV (flame condition A1)



at 230–280 Hz are mainly caused by the oscillatory behavior of the flame front.

To summarize, the flow velocity and the density contain oscillations. For instance, both quantities show peaks in the amplitude spectrum at 255 Hz. However, the spatial distribution of such fluctuations is, although sometimes similar, not identical in general. The relation between oscillations of density and flow velocity cannot be easily explained for flame flows, where reaction kinetics and temperature changes have to be taken into account (Beér and Chigier 1972; Lefebvre 1999; Poinso and Veynante 2005). Combustion oscillations grow when their energy gain from combustion is larger than the losses across the flame boundaries. These oscillations can be reduced, when the energy source term is sufficiently decreased by the boundary loss term containing flow velocity (Dowling and Morgans 2005). In order to discuss this phenomenon, pressure, density, specific heat capacities, local speed of sound and heat release rate must be taken into account. Consequently, density and velocity information are both helpful for combustion analysis. For this demand, LIV and FM-DGV measurements complement each other providing enhanced information about oscillations in flame flows.

6 Conclusions and outlook

Time-resolved measurements in flames are key for investigating flame instabilities, which is important for

achieving a stable combustion when designing burners, e.g., for aircraft engines. For this purpose, non-intrusive, robust, optical measurement techniques with a high measurement rate of several kilohertz are desired. In order to obtain flow velocity spectra, frequency modulated Doppler global velocimetry (FM-DGV) has been introduced as an appropriate measurement tool for flame flows. In addition, density spectra were acquired with laser interferometric vibrometry (LIV). Both techniques were applied to a variable geometry burner with a swirl-stabilized flame, which allows stable lean combustion over a wider range of air mass flow rates than a fixed geometry burner. This is important for novel combustion concepts with, e.g., low NO_x emissions.

At first, the flame structure was characterized by measuring CH^{*}-emissions. As a result, the attachment and detachment of the flame were observed for several burner operation conditions. The variable geometry of the burner allowed stable combustion down to 50 % lower mass flow rates than a fixed geometry. From flow field measurements with stereo particle image velocity, it could be derived further that the flame stabilizes at the place of strong velocity gradients and at the base of the swirling motion.

Furthermore, FM-DGV was successfully introduced for characterizing flow velocity oscillations in the design point (lean combustion) of the variable geometry burner. The use of a narrowband optical filter around the laser wavelength and the application of a sinusoidal frequency modulation with 100 kHz, which means evaluating harmonics of the

detector signal at 100 kHz and 200 kHz according to the FM-DGV measurement principle, make this technique almost insensitive to optical disturbances due to the flame glow. Finally, velocity amplitude spectra in the flame flow up to 2.5 kHz were measured simultaneously at multiple points. The spectra contain a peak at about 255 Hz, which is maximum 65 mm/s in the swirl region and vanishes in the flow center. A broader peak around 60 Hz with 50 mm/s amplitude dominates in the flow center.

The density spectra measured with LIV agree qualitatively well with the velocity spectra. A peak in the amplitude spectra at about 255 Hz was also found, which is related to strong combustion fluctuations. However, a comparison between density and velocity fluctuations is a complex task, because the interaction between both quantities is not always apparent. Consequently, both quantities have to be measured for the analysis of flame flows. This is possible with FM-DGV and LIV, which is a progress for research. Both techniques complement each other offering new insights into the physics of flame flows.

Despite the measured oscillations, the flame burned stable in the experiment. Hence, further operating points of the burner have to be investigated next for identifying flow conditions, which lead to flame instabilities. In addition to the evaluation of velocity spectra (temporal correlation), also the spatial correlation of the flow velocity fluctuation should be evaluated, which might be also useful for identifying and investigating flame instabilities. Furthermore, simultaneous measurements of all three velocity components are desired to resolve the temporal behavior of the entire flow velocity vector. This is possible by extending the FM-DGV system, e.g., by applying three receiving units operating in parallel.

Acknowledgments The authors thank the Deutsche Forschungsgemeinschaft (DFG project Cz 55/22-1) and the Austrian Science Fund (FWF project 24096-N24) for their financial support.

References

- Albrecht H-E, Borys M, Damaschke N, Tropea C (2003) Laser Doppler and phase Doppler measurement techniques. Springer, Berlin
- Beér JM, Chigier NA (1972) Combustion aerodynamics, 1st edn. Applied Science Publishers Ltd., Barking
- De Leo M, Saveliev A, Kennedy LA, Zelepouga SA (2003) Experimental diagnostics for the study of combustion instabilities in lean premixed combustors. *J Propuls Power* 19(5): 735–750
- De Leo M, Saveliev A, Kennedy LA, Zelepouga SA (2007) Experimental diagnostics for the study of combustion instabilities in lean premixed combustors. *Combust Flame* 149(4): 435–447
- Dowling AP, Morgans AS (2005) Feedback control of combustion oscillations. *Annu Rev Fluid Mech* 37:151–182
- Fischer A, Büttner L, Czarske J (2011) Simultaneous measurements of multiple flow velocity components using frequency modulated lasers and a single molecular absorption cell. *Opt Commun* 284:3060–3064
- Fischer A, Büttner L, Czarske J, Eggert M, Grosche G, Müller H (2007) Investigation of time-resolved single detector Doppler global velocimetry using sinusoidal laser frequency modulation. *Meas Sci Technol* 18:2529–2545
- Fischer A, Büttner L, Czarske J, Eggert M, Müller H (2008) Measurement uncertainty and temporal resolution of Doppler global velocimetry using laser frequency modulation. *Appl Opt* 47(21):3941–3953
- Fischer A, Büttner L, Czarske J, Eggert M, Müller H (2009) Measurements of velocity spectra using time-resolving doppler global velocimetry with laser frequency modulation and a detector array. *Exp Fluids* 47:599–611
- Fischer A, Büttner L, Czarske J, Gottschall M, Mailach R, Vogeler K (2010) Doppler global velocimetry with laser frequency modulation for the analysis of complex turbulent flows. Number 1.8.2, pp 1–13, Lissabon, 5–8. July 2010. 15th international symposium on applications of laser techniques to fluid mechanics
- Fischer A, Haufe D, Büttner L, Czarske J (2011) Scattering effects at near-wall flow measurements using Doppler global velocimetry. *Appl Opt* 50(21):4068–4082
- Fischer A, König J, Czarske J (2008) Speckle noise influence on measuring turbulence spectra using time-resolved Doppler global velocimetry with laser frequency modulation. *Meas Sci Technol* 19:125402 (15 S.)
- Giuliani F, Leitgeb T, Lang A, Woisetschläger J (2010) Mapping the density fluctuations in a pulsed air-methane flame using laser-vibrometry. *J Eng Gas Turbines Power* 132:0316031 (p 8)
- Giuliani F, Wagner B, Woisetschläger J, Heitmeir F (2006) Laser vibrometry for real-time combustion stability diagnostics. In: ASME Turbo Expo 2006, Barcelona, Spain. GT2006-90413
- Giuliani F, Woisetschläger J, Leitgeb T (2012) Design and validation of a burner with variable geometry for extended combustion range. In: ASME Turbo Expo 2012, Copenhagen, Denmark. GT2012-68236
- Hampel B, Woisetschläger J (2006) Frequency- and space-resolved measurement of local density fluctuations in air by laser vibrometry. *Meas Sci Technol* 17:2835–2842
- Herman GT (2009) Fundamentals of computerized tomography: image reconstruction from projections, 2nd edn. Springer, London
- Hipp M, Reiterer P, Woisetschläger J, Philipp H, Pretzler G, Fliesser W, Neger T (1999) Application of interferometric fringe evaluation software at technical university graz. In: Proceedings of SPIE, number 3745, pp 281–292
- Hipp M, Woisetschläger J, Reiterer P, Neger T (2004) Digital evaluation of interferograms. *J Meas* 36(1):53–66
- Kay SM (1993) Fundamentals of statistical signal processing: estimation theory. Prentice Hall PTR, New Jersey
- Köberl S, Fontaneto F, Giuliani F, Woisetschläger J (2010) Frequency-resolved interferometric measurement of local density fluctuations for turbulent combustion analysis. *Meas Sci Technol* 21:035302 (p 10)
- Lang A, Leitgeb T, Woisetschläger J, Strzelecki A, Gajan P, Giuliani F (2008) Analysis of a pulsated flame at intermediate pressure. In: 13th international symposium on flow visualization, Nice, France
- Lefebvre AH (1999) Gas turbine combust, 2nd edn. Taylor & Francis, New York
- Leibovich S (1978) The structure of vortex breakdown. *Annu Rev Fluid Mech* 10:221–246
- Leitgeb T, Schuller T, Durox D, Koeberl S, Woisetschläger J, Giuliani F (2013) Interferometric determination of heat release in a pulsated flame. *Combust Flame*
- Lieuwen T (2003) Modeling premixed combustion-acoustic wave interactions: a review. *J Propuls Power* 19(5):765–781

- Lira I (2002) Evaluating the measurement uncertainty: fundamentals and practical guidance. Taylor & Francis, New York
- Nori VN, Seitzman JM (2009) CH* chemiluminescence modeling for combustion diagnostics. *Proc Combust Inst* 32(1):895–903
- Poinsot T, Veynante D (2005) Theoretical and numerical combustion, 2nd edn. R. T. Edwards, Inc., Graz
- Pope SB (2000) Turbulent flows. Cambridge University Press, Cambridge
- Seitz P (2007) Photon-noise limited distance resolution of optical metrology methods. In: Osten W, Gorecki C, Novak EL (eds) Optical measurement systems for industrial inspection V, volume 6616, pp 66160D–1 – 66160D–10, Munich. SPIE conference proceedings
- Syred N (2006) A review of oscillation mechanisms and the role of the precessing vortex core (pvc) in swirl combustion systems. *Prog Energy Combust Sci* 32:93–161
- Wang S, Hsieh SY, Yang V (2005) Unsteady flow evolution in swirl injector with radial entry. I. Stationary conditions. *Phys Fluids* 17:045106 (p 13)